Detecting Small Surface Vibrations by Passive Electro-Optical Illumination

Matthew Buoni, *Toyon Research Corporation, Goleta, CA*
Wellesley Pereira, Reed Weber, *Air Force Research Laboratory, Kirtland AFB, Albuquerque, NM*
Carlos Garcia-Cervera, *Mathematics Department, University Of California, Santa Barbara*

ABSTRACT

We have performed research to understand the feasibility of using signals received by EOIR sensors to detect small vibrations in surfaces illuminated by sunlight. The vibration models consider buildings with vibrating roofs, as well as ground vibrations due to buried structures. For the surface buildings, we investigated two approaches. One involved treating the roof as an elastic medium subject to deformation resulting in a PDE whose solution describes the fluctuation in the surface's normal direction vector. The second approach treated the roof as a rigid mass subject to motion in six degrees of freedom, while modeling the dynamics of the building's frame, and tuning the parameters to result in resonant frequencies similar to real buildings. We applied the appropriate physical models of reflected and scattered light to various surfaces, specular (insulator or conductor), rough but still reflective, or diffusely scattering (Lambertian). Matlab code was developed to perform numerical simulations of any system configuration described above and easily add new models. The main engine of the code is a signal calculator and analyzer that sums the total intensity of received light over a "scene" with a variety of surface materials, orientations, polarization (if any), and other parameters. A resulting signal versus time is generated that may be analyzed in order to: 1) optimize sensitivity, or 2) detect the vibration signature of a structure of interest. The results of this study will enable scientists/engineers to optimize signal detection for passive exploitation of scattered light modulated by vibrating surfaces.

1. Introduction

Toyon Research Corporation and UCSB have developed physics-based models for reflected and scattered light from vibrating surfaces. We have modeled the vibration sources in structures and the ground, and simulated the signals received from Optical/IR sensors viewing these surfaces from space at various orientations and times of day.

In Section 2, we discuss our modeling assumptions and procedures. We address the surface reflectivity in subsection 2.1, and surface vibration models in section 2.2 (building vibrations in 2.2.1 and ground vibrations in 2.2.2). In Section 3, we describe our simulation framework developed in Matlab that calculates the temporal signal that the optical/IR sensor will receive. Our simulation is capable of modeling a wide range of parameter variations, including: 1) incoming light direction, 2) sensor viewing direction, 3) section of scene that sensor is viewing, 4) sensor polarization filter (if one is applied), 4) sensor noise level, 5) surface characteristics (diffuse or near-specular, i.e. spread, albedo or reflection coefficient), and 6) spectra of vibrations. Section 4 describes our simulation results, as we perform a series of sensitivity studies that fixes all but one or two simulation parameters at a time. Section 4.1 is applied to vibrating building structures and 4.2 to the vibrating ground. In Section 5 we conclude by summarizing our observations and providing our recommendations for maximizing likelihood of detection of small vibrations.

2. Models and Assumptions

2.1 Optical reflection properties of various materials

In order to gain insight into the methods that may be exploited for detecting surface vibrations optically, we first study what is known about light reflection from various surfaces. Consider the diagram shown in Figure 1, showing monochromatic polarized light incident upon a surface at angle, θ_i. We will assume that the incident light travels through air with index of refraction $n_1 = 1$, and the incident surface may be either an insulator or conductor. We consider three types of surfaces: 1) specular surfaces (perfectly smooth), 2) diffuse surfaces (Lambertian), and 3) real surfaces that exhibit both specular reflection and diffuse reflection. The reflectance of a surface may be characterized by its Bidirectional reflectance distribution function (BRDF), which is the ratio of *reflected power per unit solid angle per unit projected surface area perpendicular to the outgoing ray* (surface radiance) and *incoming power per unit surface area* (surface irradiance). The BRDF is a 4-dimensional function (of the incoming direction angles, (θ_i, φ_i), and the outgoing direction angles, (θ_r, φ_r)).

2.1.1 Surfaces that Reflect Specularly

First consider the case of a *perfectly smooth surface* (specular reflection), for which the solutions to Maxwell's Equations give the ratio of reflected power to incident power and are known as the Fresnel Equations. For such surfaces, all reflected energy is concentrated in one direction such that $\theta_r = \theta_i$ as shown in Figure 1, which may be represented quantitatively by the BRDF,

$$f(\theta_i, \varphi_i, \theta_r, \varphi_r) = R(\theta_i)\frac{\delta(\theta_i - \theta_r)\delta_{2\pi}(\varphi_i - \varphi_r - \pi)}{\cos(\theta_i)}, \tag{1}$$

where $\delta(\theta)$ is the Dirac delta function and $\delta_{2\pi}(\theta)$ is the Dirac delta function of period 2π, and $R(\theta)$ is the power reflection coefficient at incident angle θ.

In addition to the material index of refraction, the solution depends upon the polarization of the incident light. S-polarized light has its electric field perpendicular to the plane of the diagram in Figure 2 and thus parallel to the interface, whereas p-polarized light has its electric field in the plane of the diagram and perpendicular to the s-polarized electric field [2, 4, 14].

For insulating materials, the reflection coefficient for s-polarized light is given by the expression,

$$R_s = \left| \frac{n_1 \cos(\theta_i) - n_2\sqrt{1 - \left(\frac{n_1}{n_2}\sin(\theta_i)\right)^2}}{n_1 \cos(\theta_i) + n_2\sqrt{1 - \left(\frac{n_1}{n_2}\sin(\theta_i)\right)^2}} \right|^2, \tag{2}$$

while the reflection coefficient for p-polarized light is given by,

$$R_p = \left| \frac{n_1\sqrt{1 - \left(\frac{n_1}{n_2}\sin(\theta_i)\right)^2} - n_2\cos(\theta_i)}{n_1\sqrt{1 - \left(\frac{n_1}{n_2}\sin(\theta_i)\right)^2} + n_2\cos(\theta_i)} \right|^2. \tag{3}$$

Fresnel's equations ((2) and (3)) are plotted versus angle of incidence, θ_i, in Figure 2 for light traveling through air ($n_1 = 1$) incident upon a glass surface ($n_2 = 1.5$). For conducting materials, Fresnel's Equations may still be applied provided that we use a complex index of refraction,

$$n_2 = \sqrt{1 + i\left(\frac{\sigma}{\epsilon_0 \omega}\right)} = n_R + i\, n_I\,, \tag{4}$$

where $\sigma, \epsilon_0,$ and ω are conductivity, permittivity of free space, and angular frequency of light [6]. Physically, the imaginary part accounts for the fact that EM-radiation is attenuated as it travels through conducting materials.

2.1.2 Surfaces that Reflect Diffusely (Lambertian)

Now consider a surface that reflects diffusely. Diffuse reflection is an idealization of a limiting case for which the outgoing reflected energy is independent of the direction of the incoming light that irradiates a surface. Physically, such materials are *rough*, with a surface roughness length scale much greater than the wavelength of light reflecting from the surface [1, 9, 10]. Photons undergo multiple reflections within the facets of these rough surfaces, which acts to randomize their direction and polarization when they finally exit the surface. For example, a surface with RMS roughness of 10 μm interacting with yellow light at wavelength 589 *nm* would tend to reflect diffusely. The BRDF for these Lambertian surfaces is given by

$$f(\theta_i, \varphi_i, \theta_r, \varphi_r) = R_d, \tag{5}$$

where R_d is the diffuse surface albedo constant. The outgoing radiation intensity is the same in all directions, which means that the surface looks equally bright when viewed from any direction. Another description of Lambertian surfaces that is sometimes given is that each patch of area on the surface radiates according to "Lambert's cosine law," which states that the radiant flux from a patch of surface area ΔA is proportional to $\cos(\theta_r)$. Since the patch of area appears smaller as $\Delta A \cos(\theta_r)$ when viewed from angle θ_r, we see that the intensity (radiant flux per unit area) is actually constant and consistent with equation (5).

2.1.3 Real Surfaces that Exhibit Both Specular and Diffuse Reflection

There are many models that attempt to capture the behavior of real surfaces, which are neither perfectly specular nor perfectly diffuse. Most physically derived surface reflection models described in the literature reference the work of Torrance and Sparrow [16]. More recent models refine and extend this basic model [8, 9, 10]. These models have been validated experimentally on a small but representative group of rough and smooth surfaces, conductors and insulators. The main results of this work may be summarized as follows: real surfaces exhibit varying degrees of 1) specular spike, 2) diffuse, and 3) specular lobe (see Figure 1). The equation that describes the BRDF of these surfaces is a combination of three terms, two of which are given by equations (1) and (5) and the third term representing the specular lobe given by

$$f(\theta_i, \varphi_i, \theta_r, \varphi_r) = R(\theta_i)[G/\cos(\theta_r)]\exp\left(-\alpha^2/2m^2\right), \tag{6}$$

where *G* is a geometrical factor resulting from the surface microfacets dependent on both the incident light and viewing direction, α is the angle between the viewing direction and the center of the specular lobe (which may not be in the same direction as the specular spike), and *m* is the RMS slope of microfacets. G and α are a complex mathematical expressions that contain the additional angular dependence of the BRDF for the specular lobe, but in this paper we will use a constant *G* and specular lobe center aligned with the specular spike.

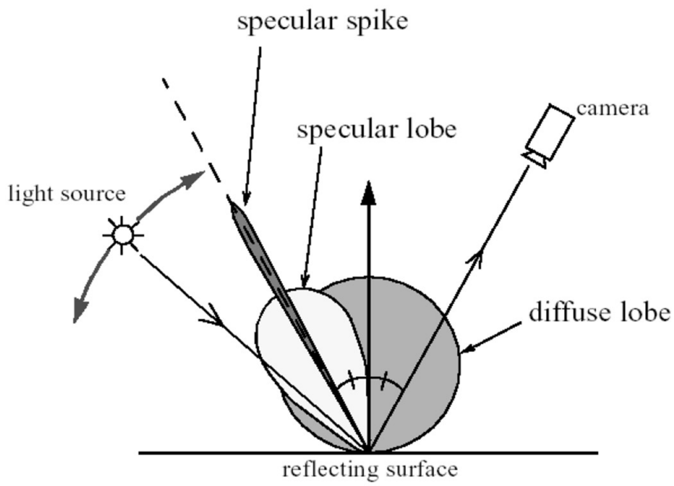

Figure 1. Types of Reflection
Specular spikes, diffuse, and specular lobe reflection models are illustrated for photons incident upon a reflecting surface.

2.2 Vibration models of surfaces

2.2.1 Vibration of building substructures

In addition to the building frame vibrations, individual substructures of the building (windows, doors, roof, etc.) may vibrate due to either mechanical or acoustical coupling from the building vibrations. A window, for example, may be modeled as a thin rectangular elastic solid subject to displacement perpendicular to the rectangular plane, i.e. the two-dimensional scalar wave equation with forcing,

$$\frac{\partial^2 u}{\partial t^2} = v^2 \left(\frac{\partial^2 u}{\partial x^2} + \frac{\partial^2 u}{\partial y^2} \right) + \frac{F(x, y, t)}{\delta\, \rho}, \tag{7}$$

where $v = \sqrt{G/\rho}$ is the shear wave speed, G is the shear modulus, and ρ is the density, F is the force per unit area, and δ is the substructure thickness. For acoustically driven vibrations, we will assume that the boundary is fixed ($u|_{\partial\Omega} = 0$) and that the rectangular plane is driven with a pressure constant over the rectangular plane and with sinusoidal variation in time, $F(x, y, t) = p_0 \cos(\omega t)$. Based on a shear modulus of 26.2 GPa and density of 2600 kg/m^3, the shear wave speed in glass is around 3100 m/s. Assuming typical window dimensions on the order of a few meters (say L = 3 m), this establishes a system time scale of around $\tau = L/v$ = 3 m/(3100 m/s) = 1 ms. Thus, if we focus on dominant vibration driving frequencies much less than around 1 kHz, then equation (7) may be reduced to a Poisson equation as the system is always in a state of quasi-equilibrium,

$$\frac{\partial^2 u}{\partial x^2} + \frac{\partial^2 u}{\partial y^2} = -\frac{p_0}{\delta\, G} \cos(\omega t), \tag{8}$$

Another way to derive this simplification is to non-dimensionalize (4) using $t' = \omega t$, $x' = x/L$ and $y' = y/L$, which gives

$$-\frac{\omega^2 L^2}{v^2} \frac{\partial^2 u}{\partial t'^2} + \left(\frac{\partial^2 u}{\partial x'^2} + \frac{\partial^2 u}{\partial y'^2} \right) = -L^2 p_0 \cos(\omega t)/(v^2\, \delta\, \rho)\,,$$

where $\frac{\partial^2 u}{\partial t'^2} \sim \frac{\partial^2 u}{\partial x'^2} + \frac{\partial^2 u}{\partial y'^2} \sim u$. And since $\omega \ll v/L$, we can ignore the $\frac{\partial^2 u}{\partial t'^2}$ term.

Another possible mode that we imagine driving the substructures of the building to vibrate is that the boundary vibrates (e.g. window frame) due to mechanical coupling of the building to the vibration source and the substructure vibrates in response to this boundary driving force. In this case, the boundary condition is given by $u|_{\partial\Omega} = A_0 \cos(\omega t)$, but no external driving force,

$$\frac{\partial^2 u}{\partial t^2} = v^2 \left(\frac{\partial^2 u}{\partial x^2} + \frac{\partial^2 u}{\partial y^2}\right). \tag{9}$$

We can transform to a Dirichlet boundary condition by defining $\bar{u} = u - A_0 \cos(\omega t)$. The result is that we obtain an equation similar to (8),

$$\frac{\partial^2 \bar{u}}{\partial x^2} + \frac{\partial^2 \bar{u}}{\partial y^2} = -\frac{\omega^2 \rho\, A_0}{G} \cos(\omega t). \tag{10}$$

Note that all the spatial shape dependence of u is contained in $\bar{u}$. Thus, $\bar{u}$ gives the amplitude of shape deformations of the subsurface due to building vibrations.

We can estimate the magnitude of the surface deformations in both cases, equations (8) and (10), simply as L^2 multiplied by the right-hand side. We estimate a sound pressure of 120 dB (20 Pa), material thickness $\delta = 1$ mm, and G = 26.2 GPa, and L = 3 m, which gives $7\mu m$ due to acoustic forcing from a 120 dB source. In the case of mechanical vibrations transmitted through the substructure frame, we estimate $\omega = 2\pi\ 50\ s^{-1}$, $\rho = 2600$ kg/m^3, $A_0 =$ 1 mm (somewhat ad hoc estimate for building vibrations), giving a surface deformation estimate of *10* μm. More precise deformation shape profiles may be obtained by solving (8) or (10) numerically. Figure 2 shows the deformation displacement and gradient obtained by solving for the steady-state solution to equation (10) on a 3m-by-3m square. Maximum displacement is around 6 μm, and maximum gradient magnitude is around 10^{-5}. The gradient magnitude is exactly the same as the magnitude of the surface normal variation and thus the magnitude of light scattering angle variations. Finally, Figure 10 shows this elastic displacement profile applied to the roof of a simple rectangular building structure, which is used in our Matlab simulation model described in section 3.

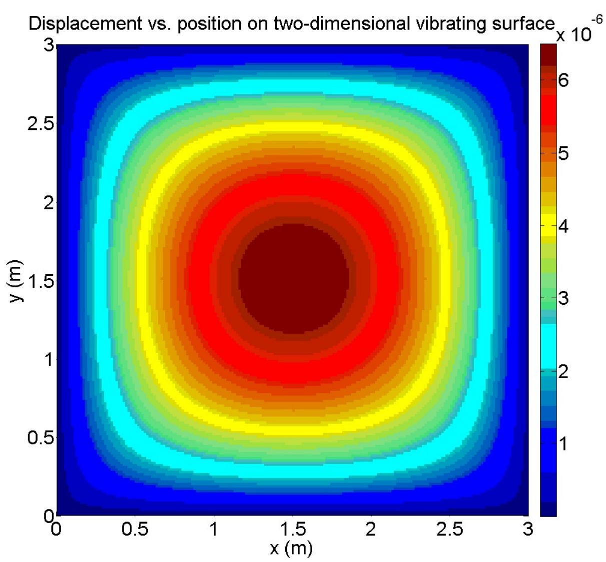

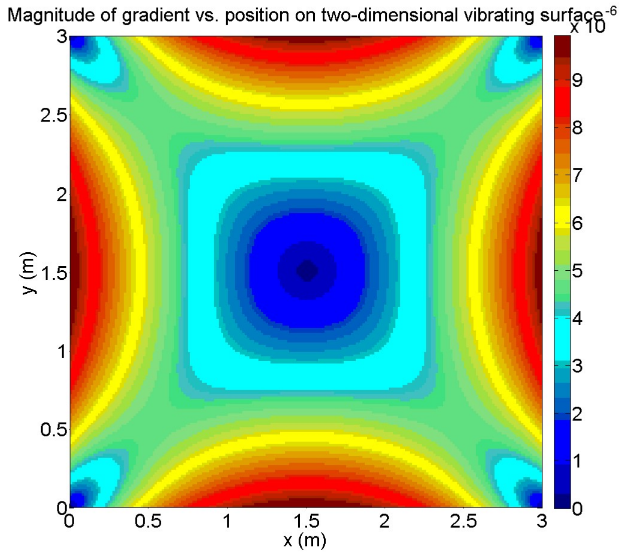

Figure 2. Surface Deformation and Gradient
Surface deformation, displacement (above) and gradient magnitude (below) for a 3m-by-3m vibrating glass surface modeled by equation (10) (solved numerically in Matlab).

While the preceding analysis gives some estimate for the magnitude and shape of surface deformations due to vibrations, some of the numerical values used may be quite different for actual structures of interest and vibration modes. In the remaining sections, we will allow these magnitudes to vary as parameters and study the feasibility of detecting these vibrations optically by light scattered from these surfaces.

2.2.2 Vibration of building frame

While our building vibration model described in section 2.2.1 captured the effects of material elasticity of a subsection of a building structure subject to forcing, it did not capture the effect of the building's resonant modes due to structural parameters of frame stiffness and damping plus building. It is these parameters that we model in this section.

Our objective is create as simple a model as possible that captures the richness of multiple building resonances that in the presence of a driving force plus noise will result in a signal with a mix of spectral components at both the resonant and driving frequencies similar to what is seen in real data [11]. To this end, a schematic of our building resonance model is shown in Figure 3. A rigid sheet of mass *M*, and dimensions *LX* by *LY* is supported at its four corners by a spring-dashpot system. Each spring-dashpot system has a stiffness k_1 and damping coefficient b_1 for vertical movements, and a stiffness k_2 and damping coefficient b_2 for lateral movements. As a driving force, we subject the base of the building at *one* corner to a circular displacement function that rotates at the driving frequencies,

$$\vec{A}(t) = \sum_i A_i\left(\cos(\omega_i t)\,\hat{d}_1 + \sin(\omega_i t)\hat{d}_2\right) \tag{11}$$

where $\hat{d}_1$ and $\hat{d}_2$ are perpendicular unit vectors in the plane of the circular driving force motion.

The motion of rigid sheet of mass, M, is described by six degrees of freedom: the three center of mass coordinates $\vec{r}_{cm} = (x_{cm}, y_{cm}, z_{cm})$, and the three Euler angles (θ, ϕ, γ), which describe the orientation of the rigid sheet's body axes, $\{\hat{e}_1, \hat{e}_2, \hat{e}_3\}$, relative to the inertial axes, $\{\hat{x}, \hat{y}, \hat{z}\}$ [13]. We adopt the convention that θ is the tilt of $\hat{e}_3$ towards $-\hat{y}$, ϕ is the CCW rotation of $\hat{e}_3$ around $\hat{z}$, and γ is the CCW rotation of the $\hat{e}_1\hat{e}_2$ plane about $\hat{e}_3$.

The forcing responsible for the system dynamics acts at each of the four corners of the rigid sheet, $\vec{r}_j$, according to the position and velocity of the corner coordinates relative to their equilibrium values, $\vec{r}_{j0}$:

$$\vec{F}_j = -(\vec{r}_j - \vec{r}_{j0}) \cdot (k_2,\ k_2,\ k_1) - (\dot{\vec{r}}_j - \dot{\vec{r}}_{j0}) \cdot (b_2,\ b_2,\ b_1), \tag{12}$$

where $\vec{r}_j$ is calculated conveniently using the body coordinate unit vectors,

$$\vec{r}_j = \vec{r}_{cm}\ \pm (LX/2)\hat{e}_1\ \pm\ (LY/2)\hat{e}_2, \tag{13}$$

for *j = 1, 2, 3, 4*. Newton's Laws of Motion for a rigid body are applied in the center of mass body coordinate system, resulting in the following differential equation system,

$$\ddot{\vec{r}}_{cm} = \textstyle\sum_{j=1}^{4} \vec{F}_j$$

$$\begin{aligned} I_1\dot{\omega}_1 &= N_1 - (I_3 - I_2)\omega_3\omega_2 \\ I_2\dot{\omega}_2 &= N_2 - (I_1 - I_3)\omega_1\omega_3 \\ I_3\dot{\omega}_3 &= N_3 - (I_2 - I_1)\omega_2\omega_1\ , \end{aligned} \tag{15}$$

where $\{I_1, I_2, I_3\}$ are the principle moments of inertial given by $M(LY)^2/12$, $M(LX)^2/12$, and $M((LX)^2 + (LY)^2)/12$, respectively. The torques, $\{N_1, N_2, N_3\}$, are expressed in the body coordinates as are the angular velocities, $\{\omega_1, \omega_2, \omega_3\}$, which are related to the Euler angles by,

$$\begin{aligned} \omega_1 &= \dot{\theta}\cos\gamma + \dot{\phi}\sin\theta\sin\gamma \\ \omega_2 &= -\dot{\theta}\sin\gamma + \dot{\phi}\sin\theta\cos\gamma \\ \omega_3 &= \dot{\gamma} + \dot{\phi}\cos\theta. \end{aligned} \tag{16}$$

Substituting equation (16) into (15) results in a 3-by-3 linear system for the Euler angle accelerations, $\{\ddot{\theta}, \ddot{\phi}, \ddot{\gamma}\}$. This system is solved at every time step in the Runge-Kutta numerical integration method applied using Matlab's *ode23* or *ode45*.

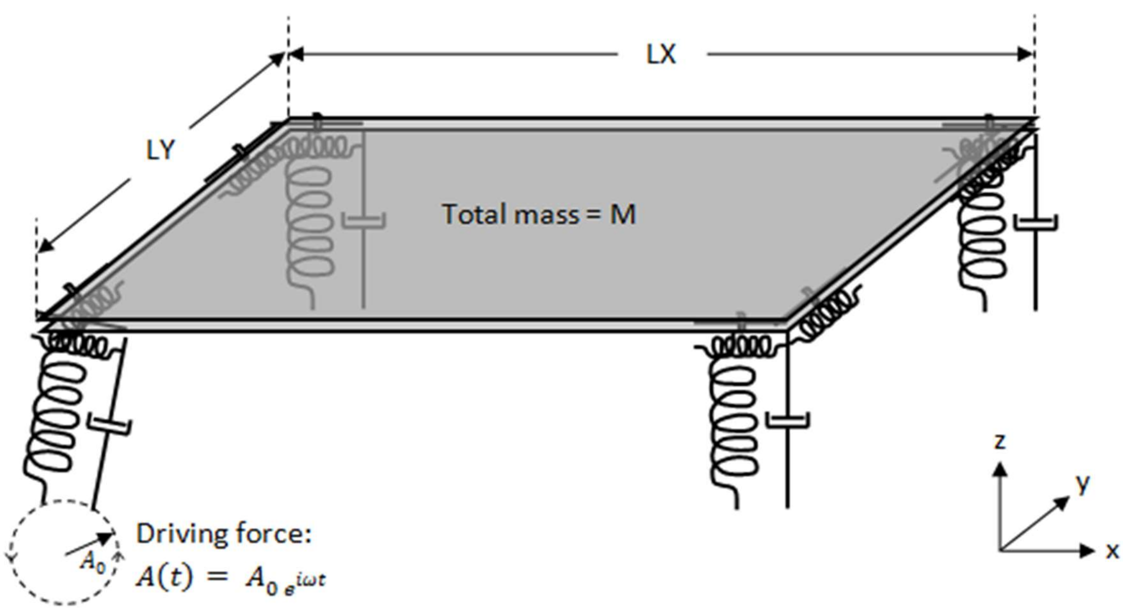

Figure 3. Building Resonance Model Schematic
Above we illustrate the mechanical system used to model building vibrations including building resonances. There is a spring-dashpot network at each of the four corners of a rigid sheet of dimensions LX by LY and mass, M. Each network provides restoring force and damping to motion in the x, y, and z-directions.

We consider a small forcing function of total amplitude $0.001m$ that acts at one of the four corners of the base of the building. The equilibrium position of this point is perturbed in a circular motion as described by equation (11) and illustrated in Figure 3. The impulse and frequency response is calculated numerically by applying a superposition of all frequencies between 0 and half the sample frequency $f_s/2$, i.e. the Nyquist frequency. Numerically, this driving force approximates an impulse train with period of 10 sec., which may be surmised by the shape of the impulse responses. We plot the system response in both the time and frequency domains for the degrees of freedom that are excited: x_{cm}, z_{cm}, and $\alpha = \theta \cos \phi$. The last angle, α, is the *signed* tilt of the $\hat{e}_3$ body axis relative to the fixed $\hat{z}$-axis. For system physical parameters, $M = 1$, $k_1 = (2\pi)^2$, $b_1 = 0.05$, $k_1 = 4(2\pi)^2$, $b_1 = 0.05$, we expect resonant frequencies of 4 Hz for x_{cm}, 2 Hz for z_{cm}, and $2\sqrt{3} \approx 3.5\ Hz$ for α, exactly as observed (see Figure 4). There is also a resonance of $4\sqrt{3} \approx 6.9\ Hz$ for variable γ (interpreted as twisting of the roof) not excited by our forcing, but excitable through random perturbations to the building's four corners considered in the next subsection.

a)

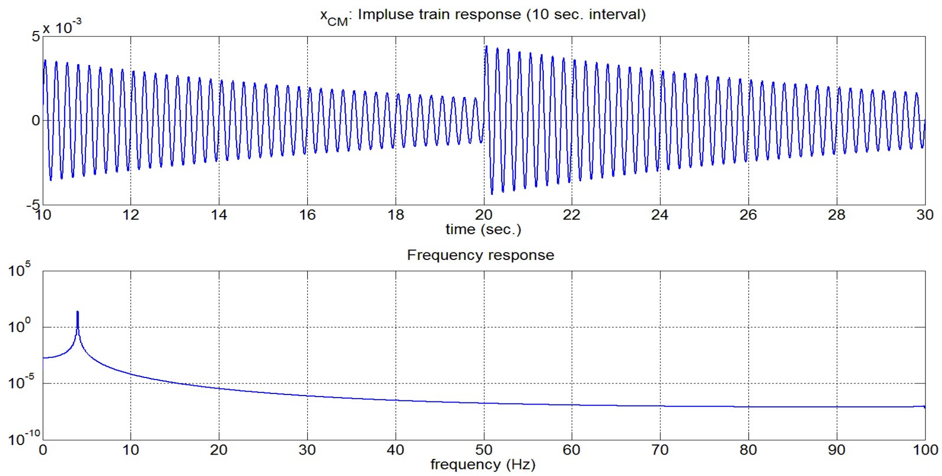

b)

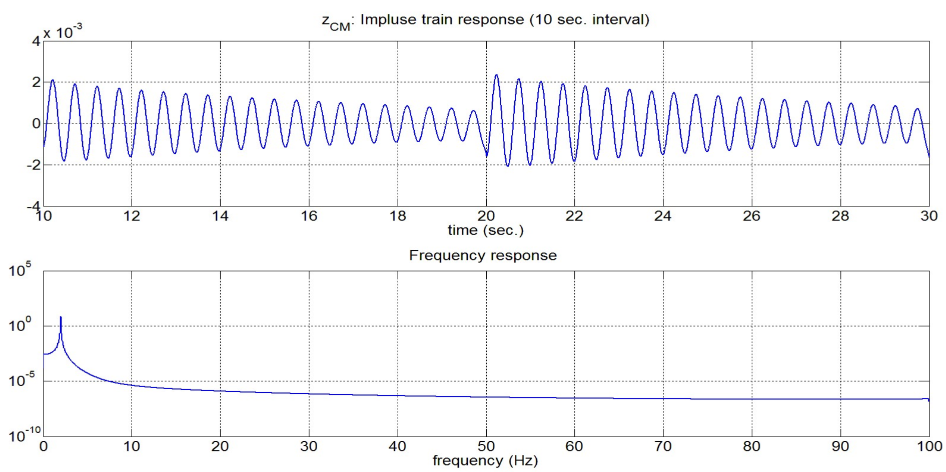

c)

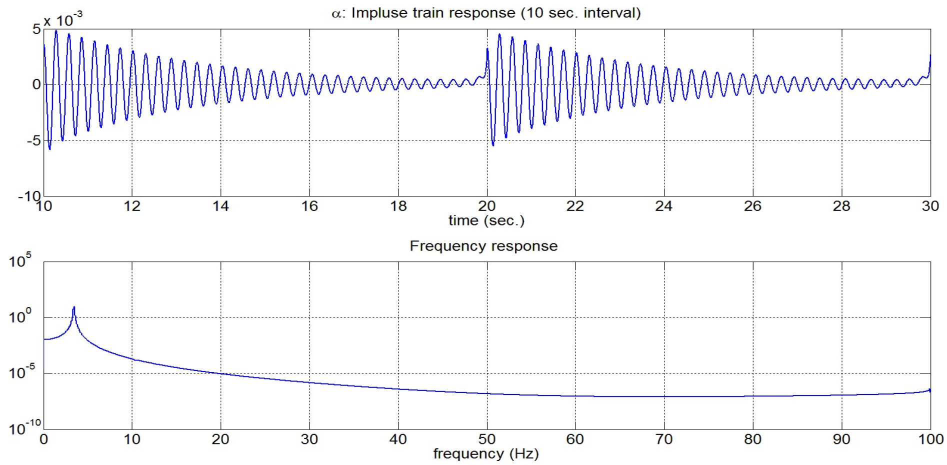

Figure 4. Building Resonance Impulse and Frequency Response
Building model impulse train response and frequency response. A driving force consisting of a superposition of equal amplitude sinusoids with minimum frequency 0.1 Hz is used to approximate an impulse train (10 sec. period). Note that the driving force is a circular displacement of just one corner of the building structure as illustrated in Figure 3. The system response in both the time and frequency domain is shown in (a) through (c) for the three affected degrees of freedom: x-coordinate of center of mass, z-coordinate of center of mass, and signed tilt angle, $\alpha = \theta cos\phi$.

2.2.3 Ground vibration model

Consider a building structure buried underground as shown in Figure 5. We assume that the building vibrates with some spectra and consider both vertical and lateral vibration modes. In both cases, the earth surrounding the building will be displaced and cause seismic waves to emanate. We expect compression waves (P-waves) to radiate parallel to the direction of the vibrations while shear wave (S-waves) will radiate in the plane perpendicular to the vibrations. Since lateral vibrations will mostly induce ground surface waves whose displacement vector is in the plane (Love or Lamb waves), we focus on vertical vibrations (as depicted in Figure 5) since these will deform the ground vertically, thus causing the surface normal direction to fluctuate as required for detection optically [3, 12]. Rayleigh waves have a wave speed of around 2-5 km/s at the surface of the earth's crust (dependent on the stiffness and mass of the rock present) and satisfy the two-dimensional wave equation,

$$\frac{\partial^2 u}{\partial t^2} = {v_R}^2\, \nabla^2 u, \tag{17}$$

where u is the ground surface vertical displacement, and $v_R \approx 3\ km/s$ is the wave speed [3]. We choose the boundary condition near the origin (directly above the underground building) so that only waves traveling radially outward result. The key observation is that we may use the Green's function solution to the wave equation in three-dimensions and superposition to form the Green's function solution to the wave equation in two-dimensions. The Green's function represents the solution to a PDE where the forcing function is located at a singular point. In three-dimensions, if we have sinusoidal forcing at the origin the resulting waveform is a radially outward traveling wave given by:

$$u_{G\_3D}(r,t) = \frac{1}{r}\cos(kr - \omega t). \tag{18}$$

We then superimpose an infinite vertical line (along the z-axis and through the origin) of these point sources to form the Green's function in two-dimensions:

$$u_{G\_2D}(r,t) = \int_{-\infty}^{\infty} \frac{1}{\sqrt{r^2+z^2}} \cos\left(k\sqrt{r^2+z^2} - \omega t\right) dz\,. \tag{19}$$

The integral in equation (19) does not have a closed form analytical solution, but may be solved numerically to whatever degree of accuracy is desired. Also, care must be applied in order to apply proper normalization since $u_{G\_2D}(r,t)$ is singular at the origin. Since we are using equation (19) to model waves emanating from a vibrating underground structure of finite size, we apply the following boundary condition to form our solution,

$$u(r,t) = \begin{cases} A_0 cos\big(\omega t - \phi(\omega)\big) & \text{if } r < R \\ C(\omega)\, u_{G\_2D}(r,t) & \text{if } r \geq R \end{cases}, \tag{20}$$

where $C(\omega)$ and $\phi(\omega)$ are determined uniquely by the requirement that $u(r,t)$ be continuous at $r = R,\ \forall t$. See Figure 6 for plots of this equation.

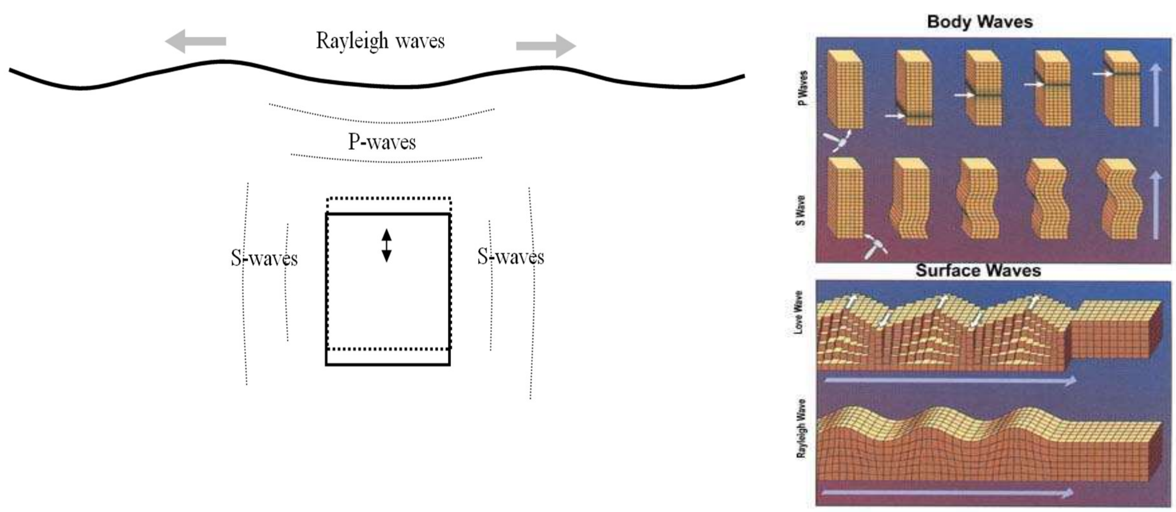

Figure 5. Ground System Scematic
To the left, a building buried underground vibrates vertically causing P-waves to travel upward and downward and S-waves to radiates to the sides. On the surface, Rayleigh waves radiate away from the point directly above the building. To the right is a pictorial representation of these seismic waves showing the ground displacements associated with each wave type.

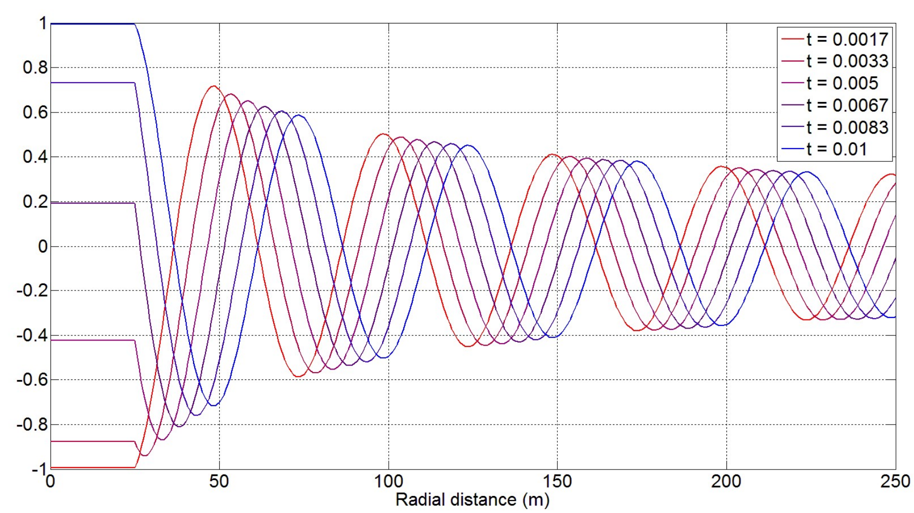

Figure 6. Ground Model Numerical Solution
Our refined ground model is shown above as: a) radial slices at a series of times over half a period of the driving force, for a driving frequency, $f = 60Hz$ and $R = 25m$.

3. Numerical Simulation of Scattered Light from Vibrating Surfaces

We have developed a detailed and efficient numerical model in Matlab that captures all the relevant physics of reflected and scattered light (discussed in section 2.1) from various surfaces. It utilizes the vibration models illustrated in Figures 2, 3, and 5 for building and ground vibrations, respectively. Our simulation outputs the signals that are received by the optical/IR sensor, and additionally allows the user to conduct sensitivity studies as one or more parameters are varied. We define *sensitivity* to be the variation in the temporal signal divided by the mean value. For a signal, $x(t)$, we define

$$S = \frac{\max\big(x(t)\big) - \min\,(x(t))}{\mathrm{mean}(x(t))}. \tag{21}$$

We assume the optical/IR sensor (or one of the sensor's pixels) is focused on a particular rectangular field-of-view (FOV) of a scene on the ground. The signal, $x(t)$, received by the sensor is defined as the average value (over the N subpixels of the scene) of the reflected intensity per unit solid angle per unit projected area, which is just the average of the BRDF, given as B in equation (23). Numerically, we calculate

$$x(t) = \frac{1}{N}\sum_{k=1}^{N} B((\hat{n}_s)_k;\ \hat{n}_i, \hat{n}_v). \tag{22}$$

where

$$B(\hat{n}_s;\ \hat{n}_i, \hat{n}_v) = \frac{\hat{n}_s \cdot \hat{n}_i\ R(\theta_i)\ C(m)\ \exp(-\alpha^2/2m^2)}{\hat{n}_s \cdot \hat{n}_v}, \tag{23}$$

Which is a numerical approximation The normal vectors are $\hat{n}_i$, the direction of the incident light source, $\hat{n}_v$ the direction of the sensor viewing the scene, and $\hat{n}_s$ the normal to the subpixel element. $R(\theta)$ is the reflectivity coefficient as a function of $\theta = cos^{-1}(\hat{n}_s \cdot \hat{n}_i)$, Φ_0 is the angular spread of the reflected light plume, and α is the angle between the light plume's center outgoing direction ($\hat{n}_s$ for diffusely scattered light, and $\hat{n}_r = 2(\hat{n}_s \cdot \hat{n}_i)\hat{n}_s - \hat{n}_i$ for specularly reflected light) and the viewing direction. $C(m)$ is a normalization constant that conserves total reflected energy. Equation (23) holds whenever all quantities in the calculation are non-negative. Otherwise, we set $B = 0$.

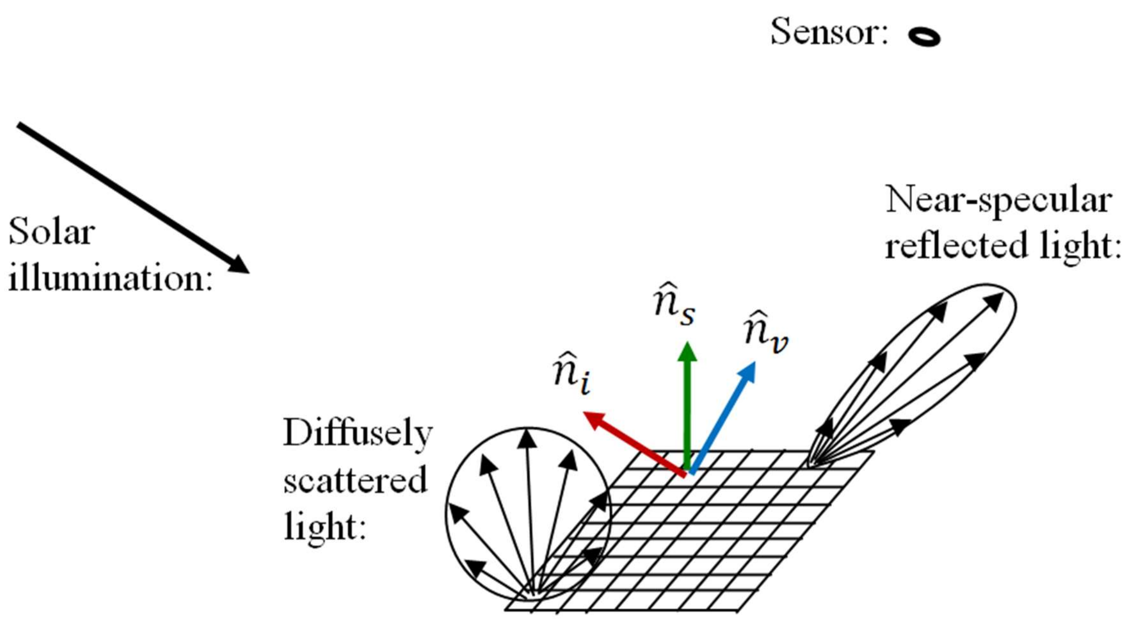

Figure 7. Matlab Scene Simulation Schematic
Shown above is a schematic of our simulation framework developed in Matlab. We assume the optical/IR sensor (or one of the sensor's pixels) is focused on a particular rectangular section of a scene on the ground. Numerically, we subdivide the scene into a matrix of subpixels each with a distinct surface normal direction, $\hat{n}_s$, and material properties (diffuse, near-specular reflection) and albedo or reflectivity function. Incorporating our building and ground vibration models causes the surface normal vectors, $\hat{n}_s$, to vary in time. The signal received by the sensor is a summation over all the BRDF values of the *N* subpixels.

4. Simulation Results and Analysis

In this section, we perform a series of sensitivity studies where we setup a scene and system configuration and vary one parameter at a time. The objective is to identify configurations that lead to higher sensitivity (as defined in equation (21)), making whatever detection algorithms that may be applied more likely to succeed. In the subsections that follow, we consider two different scenes: 1) a building above ground with a flat roof made of steel that reflects in a near-specular fashion, and 2) a building buried underground vibrating vertically inducing very small Rayleigh waves on the surface.

4.1 Building above ground, substructure vibrations (specular reflection)

We consider a rectangular building structure, 50m-by-50m, with a flat roof made of steel that vibrates at a fixed frequency, say 40 Hz, with amplitude 1 mm at the center. We assume the sun is incident at an inclination angle of $\pi/3$ rad and azimuthal angle of π rad. We position our sensor at exactly the opposite direction, $\pi/3$ rad inclination, and 0 rad azimuthal. The near-specular plume is given an angular width of 0.01 radians due the sun's finite size, subtending an angular width of the solar radius divided by the distance from the earth to the sun. The sensor focuses on the entire building roof. In Figure 8, we plot sensitivity as we perturb the sensor position from -0.02 to 0.02 rad inclination. We see that sensitivity is a minimum when the sensor is centered on the lobe and increases as we approach the edge of the lobe. In theory, if we could position the sensor perfectly on the edge of the reflected lobe, we could get sensitivities of order 1, but more generally if we can orient the sensor with approximately 0.03 rad precison, we should be able to achieve a sensitivity of order 10^{-4} with this configuration. We observed that the signals are actually at double the frequency of the vibration since every time the roof it flat (twice per vibration cycle) corresponds to a maximum reflected intensity.

Next, let's study this same system but with the sensor focused on just one quadrant of the building, so that only a quarter of the sensor's field of view is occupied by the building (see Figure 9). The rest of field of view we assume is ground that diffusely scatters light with albedo of 1, and is not vibrating. It is interesting that we can improve our sensitivity by an three orders of magnitude by simply moving our focus off-center! We can understand this result intuitively as follows. When we focus on the entire vibrating surface, there is a symmetry about the center – for every area element that is tilted slightly one way, there is another element opposite the center perturbed the opposite way. These two opposing perturbations tend to have a cancellation effect. Thus, if we can isolate just one of them, we can greatly enhance sensitivity.

Now that we have identified the two important parameter optimizations for the near-specularly reflective building, namely 1) focusing on a quadrant, and 2) viewing at an angle off the main specular lobe (by around 0.015 rad as observed in Figures 8 and 9), we continue by studying the effect of vibration amplitude on both the signal structure and resulting sensitivity. In Figure 14, we see that as the sensitivity and vibration amplitude are related approximately linearly until the sensitivity begins to saturate at order 1. This is due to vibration being so large that the signal goes to near zero over part of the cycle as the full angular width of the reflected plume is reflected completely away from the sensor.

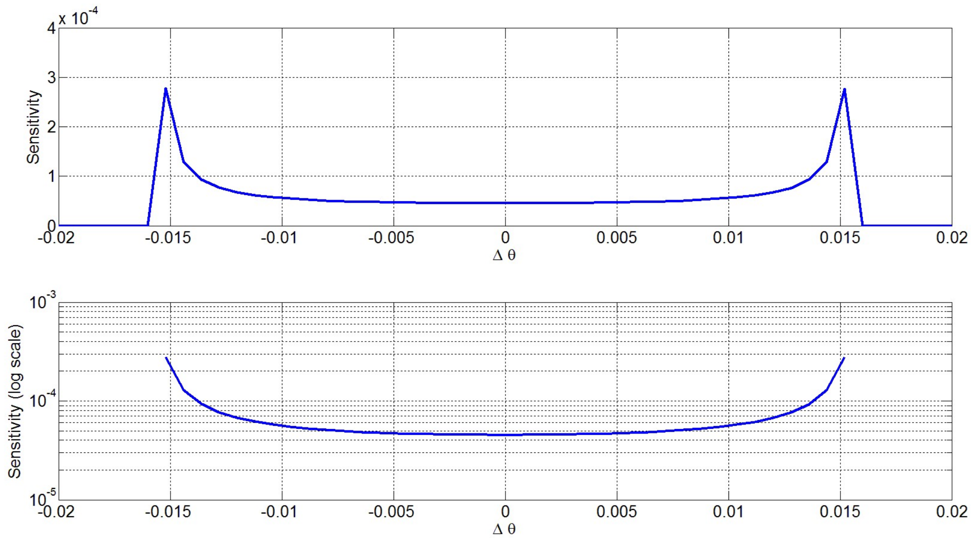

Figure 8. Building Model Signals and Sensitivity Versus Viewing Angle: Centered FOV
Sensitivity is plotted for varying sensor inclination in the reflecting building scene with sensor *centered* on building.

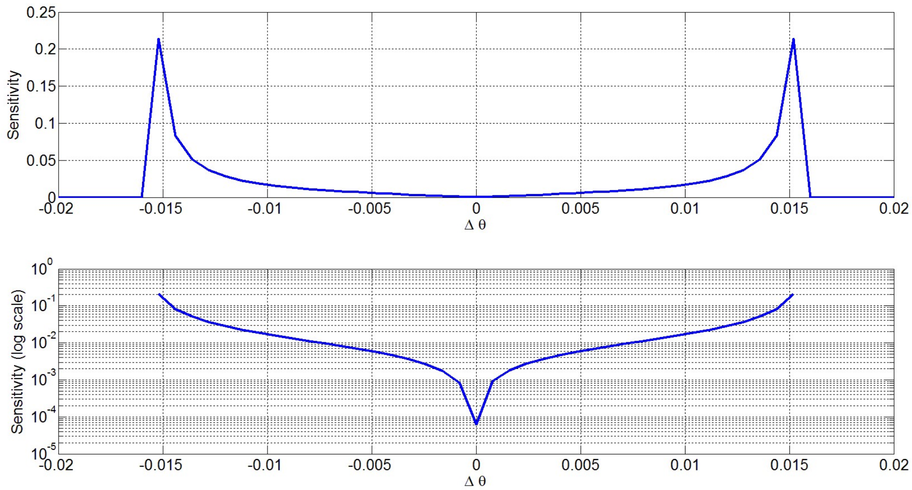

Figure 9. Building Model Signals and Sensitivity Versus Viewing Angle: Quadrant FOV
Sensitivities is plotted for varying sensor inclination in the reflecting building scene with sensor focused on one *quadrant* of building.

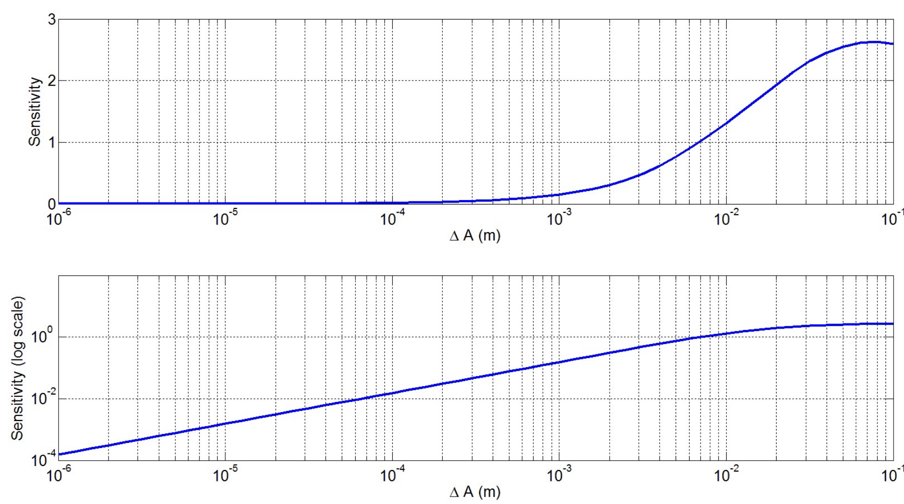

Figure 1. Building Model Signals and Sensitivity Versus Amplitude: Centered FOV
Sensitivities is plotted for varying sensor vibration amplitude in the reflecting building scene with sensor focused on one *quadrant* of building and viewed at an inclination angle 0.015 rad off the main specular lobe center.

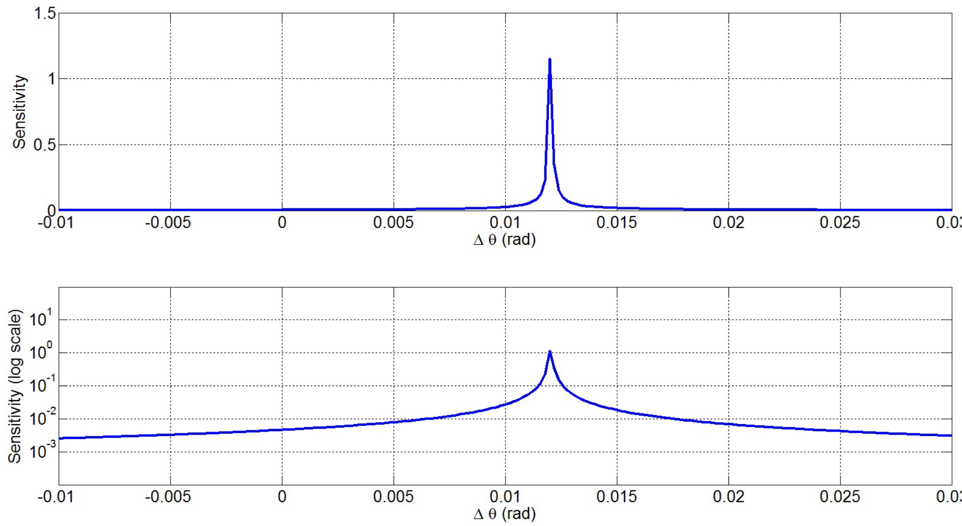

Figure 11. Sensitivity Versus Angle For Polarized Sensor Near Brewster's Angle
Sensitivity for a near-specularly reflective pane of glass viewed near Brewster's angle with a polarization filter that passes only p-polarized light. Note that the same system without polarizer has a sensitivity of around 3e-5.

We study one more near-specularly reflective system configuration more out of curiosity than practicality. We consider a square pane of glass vibrating in the same way as the roof of the previous studied building, with 1 m side length and 10 μm amplitude. We focus our sensor on a quarter of the pane, and apply a polarization filter to our sensor so that only p-polarization is sensed, while varying the incoming light angle near Brewster's angle (approximately 57 degrees, the angle at which the p-polarization component goes to zero). Our sensor is directed at the center of the reflected lobe. Sensitivity is plotted in Figure 11, showing a spike of order 1 exactly at Brewster's angle and a region of sensitivity greater than 0.01 over a window ± 0.005 rad of Brewster's angle. We note that this same system without polarizer would have a sensitivity of 3e-5. This is a huge enhancement of sensitivity of at least three orders of magnitude!

4.2 Building above ground, frame vibrations (specular reflections)

We now use the building resonance model described here to simulate the signal received by an optical/IR sensor in space. The forcing function consists of a single $10Hz$ circular motion of amplitude $0.001m$ as well as Gaussian white noise of RMS magnitude $10^{-4}m$ acting at each corner and in each dimension of motion. The driving frequency was selected to be different enough from the resonance frequencies to be resolved but small enough to be well resolved over a sampling frequency of $f_s = 200Hz$. We chose white noise for its uniform spectrum which is able to excite all the resonance frequencies of the building, similar to what we expect to happen due to wind and/or a lack of perfect smoothness in the driving frequency.

The roof surface is assumed to be made of steel giving a near-specular reflection with a spread angle of 0.01 rad due to the finite size of the sun, exactly the system studied in the elastic roof model of section 4.1. The incoming light from the sun is at angle of $\theta_i = \pi/3$ above the horizon and is viewed at the same inclination angle shifted azimuthally by π. As we did in section 4.1.1 with our elastic roof building model, we simulate this system for a series of perturbations, $\Delta\theta$, in the viewing inclination angle, i.e. $\theta_v = \theta_i + \Delta\theta$. Observed signals in both the time and frequency domain are shown in Figure 24. We see in every case there are components at both the building resonance frequencies, $3.5Hz$ in particular since this is the resonance of the tilt angle which most directly affects the surface normal vector orientation $\hat{n}_s = \hat{e}_3$, and the driving frequency $10Hz$.

a)

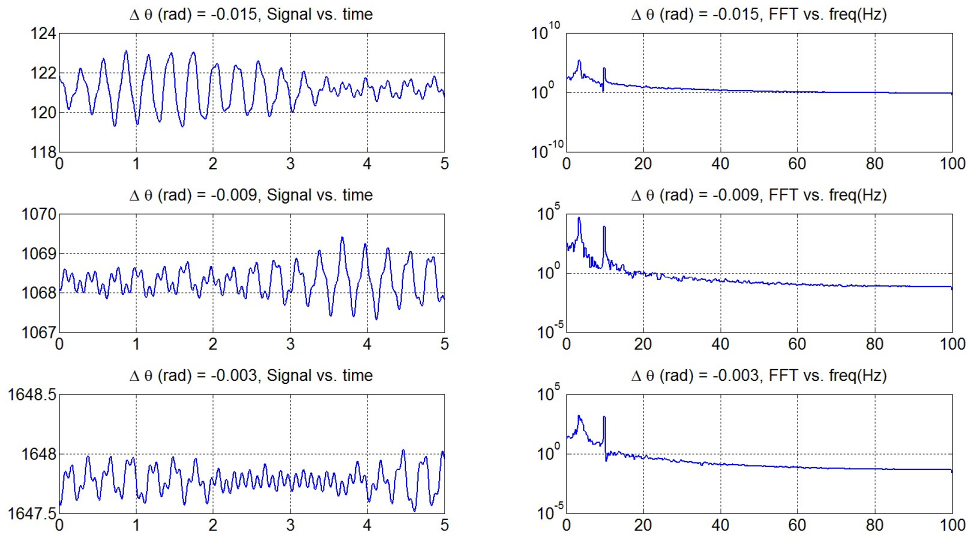

b)

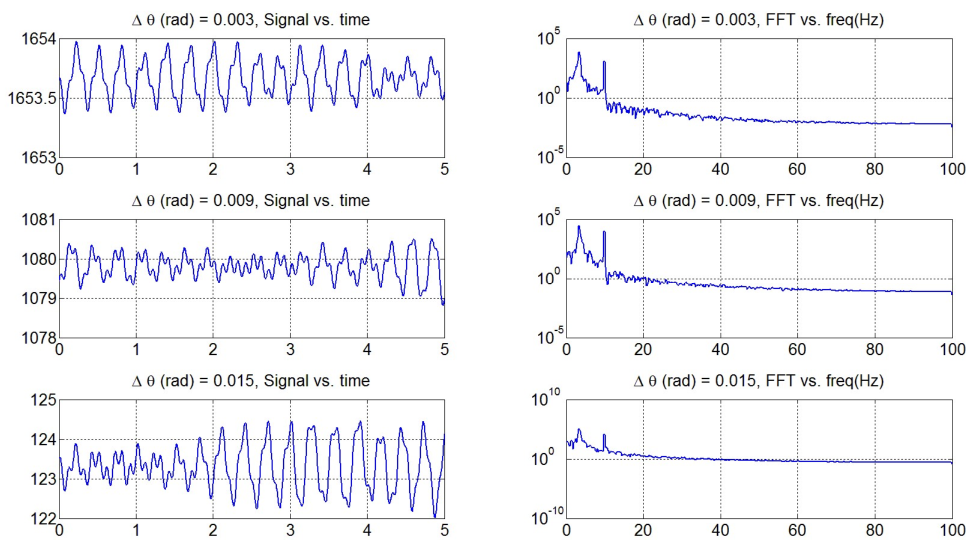

Figure 12. Building Resonance Model Signals Versus Viewing Angle
Building Resonance model signals and FFT magnitude for a driving frequency of $10Hz$ of amplitude 0.001m acting at one corner, and Gaussian white noise of RMS amplitude $10^{-4}m$ acting at all corners.

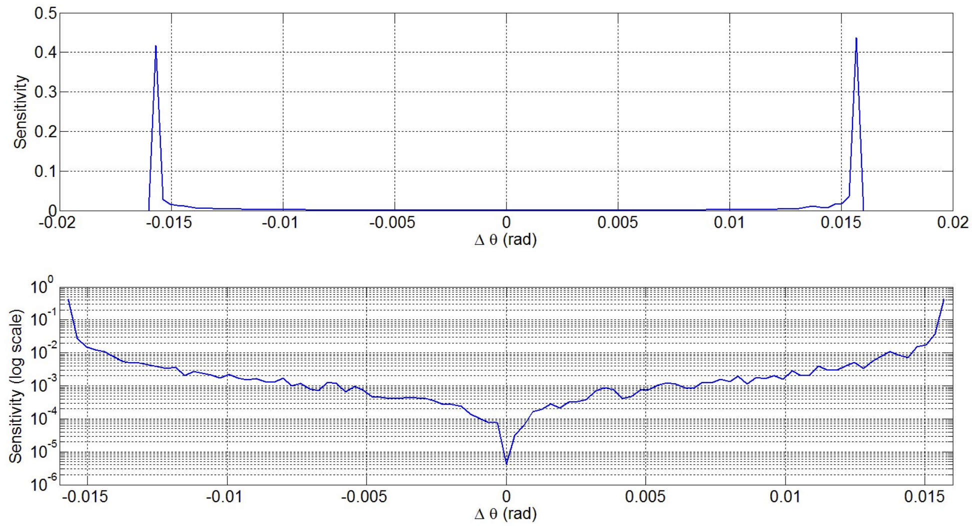

Figure 13. Building Frame Vibration Model Sensitivities Versus Viewing Angle
Building Frame Vibration Model Sensitivity, for a driving frequency of 10Hz of amplitude 0.001m acting at one corner, and Gaussian white noise of RMS amplitude $10^{-4}m$ acting at all corners.

4.3 Building underground (ground vibrates, light scatters diffusely)

We consider a building underground that causes the ground above to vibrate with some small amplitude of 1 mm. As described in Section 3.4, Rayleigh waves are created on the surface in the form described by equation (20). For a single frequency, $f_i = 40\ Hz$, we calculate a wavelength $\lambda_i = v_R/f_i = 3000/40$ = 75 m.

After having learned from the results of the building system described in Section 4.1 that sensitivity is enhanced by focusing on a quadrant of the scene to break symmetry, we start with this configuration for the vibrating ground system. Since the ground scatters light diffusely, we begin our parameter study by fixing the viewing angle at $\pi/3$ rad inclination, and 0 rad azimuthal, while varying the incoming solar illumination from 0.01 to $\pi/2$. Plots of sensitivities are given in Figure 14. We see that the lower the inclination angle of the sun in the sky, the higher the sensitivity. We can understand this result since the projected area of each surface element in the direction of the sun changes by the greatest relative amount when the sun is low in the sky. For sensor hardware sensitivity threshold in the range of 1e-4, we deduce that the sun should be lower than around 0.15 rad inclination in order for these vibrations to be detectible.

Next, we vary the width of our FOV and hold the solar inclination fixed at 0.01 rad. We find a maximum sensitivity of around 5e-3 at around 24 m wide field of view (or ~1/3 the dominant Rayleigh wavelength), as shown in Figure 15.

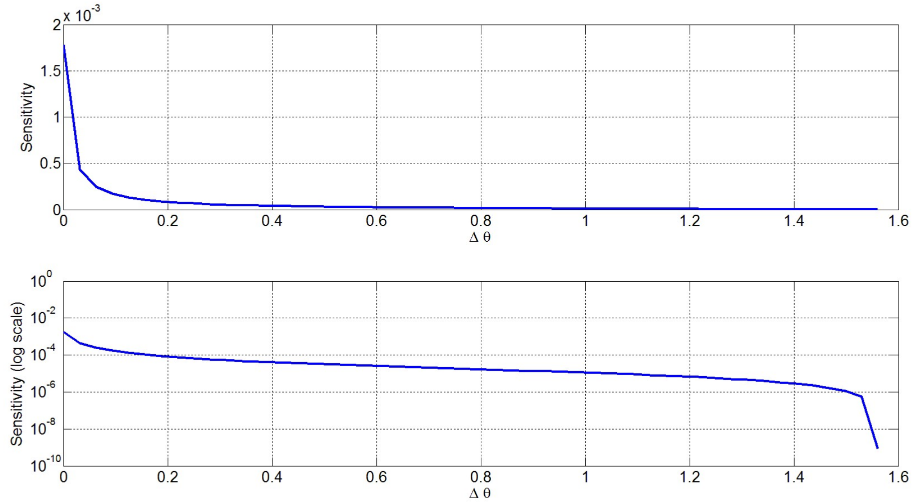

Figure 14. Signals and Sensitivity Versus Solar Inclination For Ground System
Sensitivities are plotted for varying incoming solar inclination angle for ground vibrating scene with sensor focused on one *quadrant*. FOV dimensions are 50 x 50m.

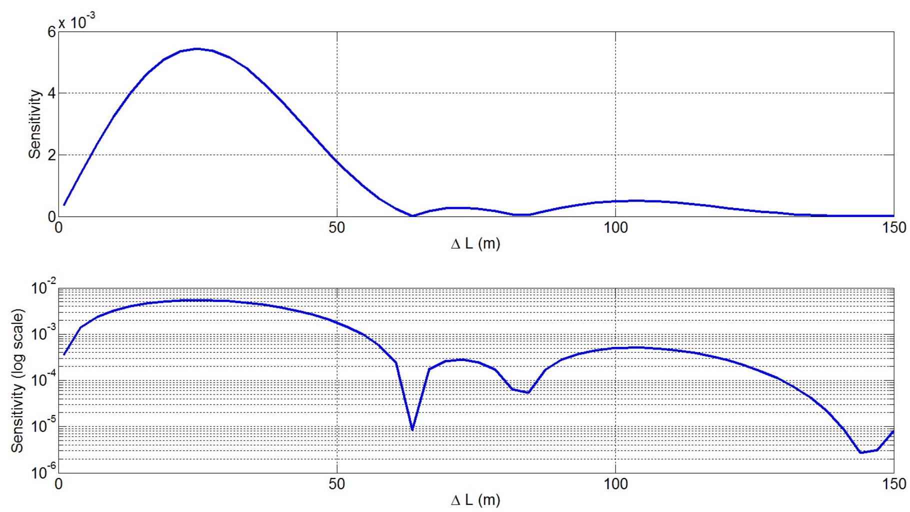

Figure 15. Signals and Sensitivity Versus FOV Width For Ground System
Sensitivities are plotted for varying width of field of view for ground vibrating scene with sensor focused on one *quadrant*. Incoming sun inclination angle is 0.01 rad.

5. Conclusions

We have created a detailed numerical model that simulates signals generated from passively reflected light from varying types of surfaces. We studied two systems in detail, a near-specularly reflecting building top and a diffusely scattering ground system subject to Rayleigh waves created by an underground vibrating structure. We have learned that it is important to break symmetry by focusing on a quadrant of the system of interest to prevent cancellation effects that greatly diminish the variation in the observed signal. One thing this points to is that we need sufficient sensor resolution such that, ideally, a pixel is focused on one quadrant of a building. Also, if the sensor resolution was very high, then algorithms could automatically combine signals from collections of multiple pixels in a near-optimal way. Additionally, observing a near-specularly reflective surface off the center of the lobe further enhances the contrast in the observed signal, since the gradient of the surface's BRDF has its largest magnitude off center. Additionally, it may be possible to utilize a polarization filter in order to enhance sensitivity when light reflects off an insulator (like glass) at Brewster's angle. In practice, this would require such a high precision in both the incoming light and viewing angle that it would most likely be impractical. For the diffusely scattering ground vibration system, we found that the lower the inclination angle of the sun in the sky, the higher the sensitivity. Furthermore, knowledge of the dominant vibration frequency would help to set the optimal width field of view at around 1/3 the corresponding Rayleigh wavelength.

References

[1] Bennett, H.E and J.O. Porteus, "Relation between surface roughness and specular reflectance at normal incidence." *Journal of the Optical Society of America* 51(2): 123-129 (February 1961).

[2] Born, Max and Emil Wolf, Principles of Optics, 7th Edition. Cambridge: Cambridge University Press. ISBN 0-521-642221 (1999).

[3] E. Bullen and Bruce A. Bolt, An Introduction to the Theory of Seismology, 4th ed. (1993).

[4] Chen, Hsi-Shu and C.R. Nagaraja Rao, Polarization of light on reflection by some natural surfaces. *British Journal of Applied Physics* 1(2): 1191-1200 (1968).

[5] Hughes, Michael et. al., "Experimental validation of building vibration propagation using a four story laboratory model." *American Society of Civil Engineers: Structures 2008 Conference*. (April 2008).

[6] Lazanyi, Istvan and Laszlo Szimay-Kalos, "Fresnel Term Approximations for Metals." SHORT papers proceedings, WSCG 2005. Plzen, Czech Republic: UNION Agency-Science Press. ISBN 80-903100-9-5 (2005).

[7] Maxwell, J.R. et. al., "Polarized Emittance. Volume I: Polarized bidirectiona reflectance with Lambertian or non-Lambertian diffuse components." *Ballistic Research Laboratories* (May 1974).

[8] Nayar, Shree K., Xi-Sheng Fang, and Terrance Boult, "Removal of specularities using color and polarization." *Proceedings of the IEEE Conference on Computer Vision and Pattern Recognition*. pp. 583-590 (1993).

[9] S. K. Nayar, K. Ikeuchi, K., and T. Kanade, "Surface Reflection: Physical and Geometrical Perspectives," *IEEE Transactions on Pattern Analysis and Machine Intelligence*, Vol.13, No.7, pp.611-634 (July 1991).

[10] Oren, Michael and Shree K. Nayar, "Diffuse reflectance from rough surfaces." *Proceedings of the IEEE Conference on Computer Vision and Pattern Recognition*. pp. 763-764 (1993).

[11] Pereira, Wellesley, et. al., "Hypertemporal Imaging Diffuse Modulation (HTI-DM) Experiment: Summary of physics and field experiments." Technical Report AFRL-RV-PS-TR-2012-0074. *Air Force Research Laboratory, Space Vehicles Directorate* (5 March 2012).

[12] Skipp, B.O., Ground Dynamics and Man-made Processes, The Institution of Civil Engineers, London (1998).

[13] Symon, Keith R., "Mechanics", 3rd ed., Addison-Wesley Publishing Co. (1971).

[14] Tan, Robby T., "Specular Reflection and Specularity." Encyclopedia of Computer Vision. Springer. ISBN 0387307710 (2012).

[15] A. Tartakovsky, A. P. Brown, and J. H. Brown, "Enhanced Algorithms for EO/IR Electronic Stabilization, Clutter Suppression, and Track-Before-Detect for Multiple Low Observable Targets," *AMOS Conference* (2009).

[16] Torrance, K.E. and Sparrow, E.M., "Theory for off-specular reflection from roughened surfaces," *Journal of the Optical Society of America* 57(9): 1105-1114 (September 1967).